Experimentally identified models of McKibben soft actuators as primary movers and passive structures

Preprint · January 2020

DOI: 10.13140/RG.2.2.31749.29920

4 authors, including:

Gina Olson
Carnegie Mellon University
17 PUBLICATIONS **128** CITATIONS
SEE PROFILE

Holly Manjarrez
Sierra Nevada Corporation
2 PUBLICATIONS **1** CITATION
SEE PROFILE

Experimentally identified models of McKibben soft actuators as primary movers and passive structures

Gina Olson*
Collaborative Robotics and Intelligent Systems (CoRIS) Institute
Oregon State University
Corvallis, OR 97331
Email: olsongi@oregonstate.edu

Holly Manjarrez
Collaborative Robotics and Intelligent Systems (CoRIS) Institute
Oregon State University
Corvallis, OR 97331
Email: manjarrh@oregonstate.edu

Julie A. Adams
Collaborative Robotics and Intelligent Systems (CoRIS) Institute
Oregon State University
Corvallis, OR 97331
Email: julie.a.adams@oregonstate.edu

Yiğit Mengüç
Collaborative Robotics and Intelligent Systems (CoRIS) Institute
Oregon State University
Corvallis, OR 97331
and
Facebook Reality Labs
Redmond, WA 98052
Email: yigit.menguc@oregonstate.edu

Soft robots join body and actuation, forming their structure from the same elements that induce motion. Soft actuators are commonly modeled or characterized as primary movers, but their second role as support structure introduces strain-pressure combinations outside of normal actuation. This manuscript examines a more complete set of possible strain-pressure combinations for McKibben actuators, including passive extension, passive compression, pressurized extension and compression of a pressurized actuator beyond the maximum actuation strain. Each region is investigated experimentally, and empirical force-displacement-pressure relationships are identified. Particular focus is placed on ensuring empirical relationships are consistent at boundaries between an actuator's strain-pressure regions. The presented methodology is applied to seven McKibben actuator designs, which span variations in wall thickness, enclosure material and actuator diameter. Empirical results demonstrate a trade-off between maximum contraction strain and force required to passively extend. The results also show that stiffer elastomers require an extreme increase in pressure to contract without a compensatory increase in maximum achieved force. Empirical force-displacement-pressure models were developed for each variant across all the studied strain-pressure regions, enabling future design variation studies for soft robots that use actuators as structures.

1 Introduction

Soft robots made of fluid-driven actuators join body and actuation, relying on the same soft actuators that deform the

*Address all correspondence to this author.

robot to support external loads. This combination of structure and actuation is inherent to the function of many soft robots, which rely on compliance to disperse force, conform to surfaces and handle delicate objects safely. Soft grippers and arms are robust solutions because they conform without exerting excessive force, but this ability is incongruous with rigid supports [1, 2]. The *actuation region*, or the load-pressure combinations which produce strain and force in the intended direction, is well studied, and experimental and analytical models exist to predict behavior [3–5]. However, there exists no guarantee that soft actuators will always be used in the actuation region. Arms or grippers under load may be pushed or pulled beyond their maximum stroke and into a state of pressurized compression or extension. Multi-directional soft arms combine two or more actuators [6–9], and arm behavior is dictated by the combination of the pressurized and passive (i.e., unpressurized) actuator reaction forces. This unification of robot body and primary mover requires an actuator behavior model that covers a more complete set of strain-pressure states in order to accurately predict soft robot behavior under internal and external loads.

Soft arms are commonly modeled with rod and beam theories that rely on an actuator or material stiffness characterization. Existing techniques rely on actuator behavior simplifications focused on the actuation region [10], or empirically determine stiffness of a complete soft arm. These techniques, while sufficient in limited cases, are not generalizable across designs and cannot predict when the actuator ceases to function as an actuator. Many bending models consider only uniaxial forces [10–13], but even a uniaxial force model must consider the possible strain and pressure permutations. Prior work applied a limited passive and actuated piecewise stiffness characterization to soft arm bending under no load [14], but did not consider all strain states.

A fluid-driven actuator's *uniaxial response space* encompasses the reaction force at all feasible combinations of uniaxial strain and pressure. Figure 1(a) illustrates a McKibben actuator's uniaxial response space. *Passive lines*, when the actuator is unpressurized, lie along the x-axis. External loads, from the environment or other actuators in the robot, cause passive deformations. *Pressurized compression* may occur when a compressive load is placed on a maximally contracted actuator, while *pressurized extension* can occur when a tensile load greater than the blocked force is applied.

A methodology for experimentally identifying the actuator reaction force in each region of the response space is demonstrated. The methodology is applied to McKibben actuators, a subset of fiber-reinforced, fluid-driven actuators. McKibben actuators are representative of general fluid-driven actuators, which all have an actuation region, a passive region and can be deformed opposite their actuation direction. Variants may extend, twist or bend and their particular actuation direction determines the response space layout. Standard McKibben actuators are studied because they produce higher forces than extending variants [15] and remain popular in soft arms and grippers [13, 16]. McKibben actuators are composed of a cylindrical elastomeric enclosure (e.g., silicone, rubber, polyurethane) that is wrapped by a braided set of fibers with a helix angle below 54.7°, as measured from the helix axis [3]. Each actuator is a heterogeneous structure, where the geometry and properties of the tube and sheath determine the location of features in the response space, such as the maximum contraction strain ε_{limit} or the maximum extension strain ε_{max}.

Existing force-displacement-pressure relationships for McKibben actuators focus on the actuation region. Three modeling techniques have been used: analytical, numerical and experimental. Simple analytical actuation region models neglect losses to the elastomeric tube and sheath and are often derived from principles of virtual work or energy conservation [3, 17, 18]. Later analytical models included losses to the tube and sheath [3] and end effects [4, 5, 19]. Analytical models generally make domain-specific assumptions (e.g., the tube is in contact with the sheath) that are violated in other states (e.g., compression). A few analytical models include pressurized extension, but no analytical model has been validated for all the strain-pressure regions analyzed in this manuscript. Finite element, or numerical, models also focus on the actuation region [20]. Finite element models require detailed material data, are slow to solve and often also assume that the sheath is in perfect contact with tube.

Experimental fits are not as informative as physics-based models, but they can be more accurate because they are derived by measuring actuator force directly. Empirical fits generally cannot be extrapolated to different actuator designs or beyond the tested domain. The simplest experimental characterizations test free contraction, blocked force or stiffness at a single pressure [9, 15]. Multiple force-displacement-pressure models have measured forces at actuation strain-pressure combinations [3, 21–23]. Experimental methods are not inherently limited to the actuation region, but there exists no systematic experimental identification of a McKibben actuator's complete uniaxial response space.

The idea of experimental model identification is extended to *passive extension*, *pressurized extension*, *passive compression* and *pressurized compression*, as a primary contribution. The developed models are intended for use in building models of more complex soft robots, specifically those that deform constituent actuators out of the actuation region (e.g., soft arms). Experimental identification provides an inherent measure of accuracy and simplicity. Elastomer and sheath material properties are not required, nor are friction coefficients or sheath braid parameters. While experimental actuator characterizations are specific to each actuator design, the characterizations can be combined with bending models to allow design studies of soft arms with any number or arrangement of actuators. Seven McKibben designs with varying wall thickness, tube material durometer and actuator diameter are examined. Each design is fit to the same model forms. The developed model forms assume length independence, which is explored experimentally, and are guaranteed to be continuous at region boundaries.

Section 2 describes a McKibben actuator's response space. Section 3 describes methods. Sections 4.1-4.2 quantify potential variances from time, history and length dependencies. Region fits and design comparisons are reported in

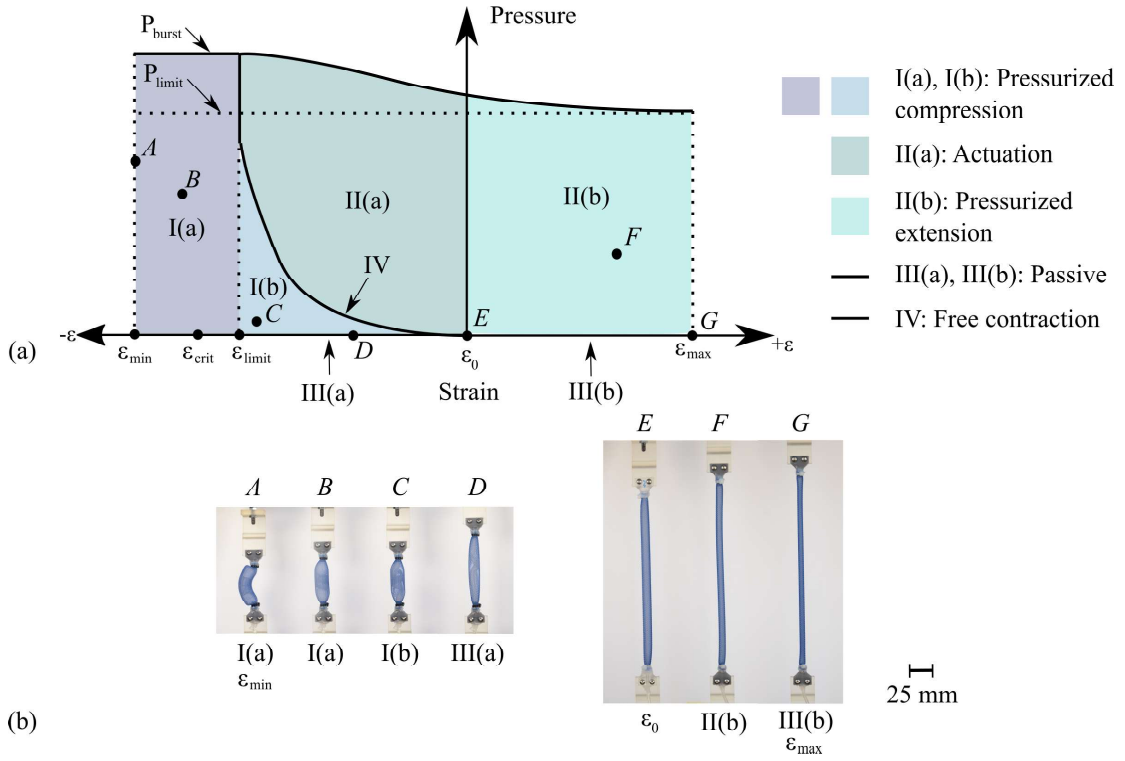

Fig. 1. (a) The uniaxial strain-pressure response space of a McKibben actuator. Forces are measured in the perpendicular plane, and colors indicate regions of the response space. Solid lines represent physical features or limits (e.g., P_{burst}), while dotted lines represent practical or user-imposed limits (e.g., P_{limit}). The illustration is not to scale. (b) Examples of a McKibben actuator in the indicated regions. Letters and dots in (a) indicate approximate locations of sample states. Region II and III(b) are demonstrated on 200 mm long actuators and Regions I and III(a) are demonstrated on 100 mm long actuators.

Sections 5.1-5.4. Section 6 discusses applicability and future work. Appendix A describes actuator manufacturing.

2 Strain-pressure regions

A fluid driven actuator's reaction force depends on the actuator's strain and pressure. Each actuator's response space is divided into strain-pressure regions. The size, shape and layout of these regions depends on the actuator type. McKibben actuators have actuation regions to the left of zero strain, while extending actuators have actuation regions to the right of zero strain. Figure 1(a) shows a McKibben actuator's response space, with examples of actuators in key regions shown in Figure 1(b). Solid lines represent physical, measurable features (e.g., the free contraction line) of the response space, while dotted lines represent practical or imposed limits (e.g., user-imposed maximum strain).

Practical and user-imposed limits determine the response space's outer shape. Empirical methods rely on copious test data, and improperly selected limits will damage specimens before testing concludes. Limits can be identified with destructive testing, but they can be more quickly estimated via observation, consideration of system practicalities and engineering judgement. McKibben actuator limits are:

• P_{limit}, P_{burst}: The actuator's maximum pressure is divided into a true burst pressure P_{burst} and a user-selected maximum operation pressure P_{limit}. P_{burst} varies by strain and, while measurable, is an impractical limit because each characterization test would be destructive. P_{limit} is ideally lower than P_{burst} at any strain. P_{limit} was set as 110 kPa (16 psi) for DS10-4-1 (Table 1) and 68.9 kPa (10 psi) for all other variants, based on trial and error; higher pressures occasionally caused separation between actuator caps and tubes. Dragon Skin 10 is stiffer and requires higher actuation pressures.

• ε_{min}: The user-selected largest compressive strain, which was set to a constant 55%. Larger compressive strains wrinkled some sheaths.

• ε_{max}: The user-selected maximum strain is the largest allowable extension strain. McKibben actuators are compliant when initially extended, and they stiffen quickly as the strain increases. A low maximum strain will fail to capture the change in stiffness, but large extension strains (or forces) applied repeatedly may damage an actuator at strains lower than the break strain. ε_{max} was set as the strain that produced a 12.5 N tensile reaction force, which was sufficient to observe the change in stiffness for all tested actuators.

The response space's shape and features are driven by the actuator's physical design, and region boundaries were placed where the dominant physics changed (e.g., during actuation, the tube contacts the sheath, resulting in contraction and a tensile force, but during pressurized compression, the tube may not contact the sheath and the force is compres-

sive). The features and regions are:

• ε_{limit}: The limit strain represents the maximum actuation strain achievable by P_{limit}. ε_{limit} is not necessarily the nominal maximum stroke of an ideal McKibben actuator, which may only be reached at pressures over P_{limit}. The limit strain ε_{limit} divides Region I into Region I(a) and Region I(b).

• ε_{crit}: The critical strain represents the theoretical maximum stroke, and it may be estimated by calculating the strain that produces a fiber angle of 54.7° [3]. When pushed beyond the critical strain, a standard, contracting, McKibben actuator will behave like an extending McKibben actuator.

• *Region I(a)*: The actuator is pressurized but compressed beyond ε_{limit}, which is referred to as pressurized compression. The actuator force in this region is compressive and, for $\varepsilon < \varepsilon_{crit}$, pressure increases force magnitude.

• *Region I(b)*: The actuator is contracted less than the limit strain, but the pressure is too low to overcome the force required to deform the sheath and elastomeric tube. Like Region I(a), Region I(b) is a form of pressurized compression, but the actuator is under-inflated. The actuator force is compressive, but pressurization decreases force magnitude.

• *Region II(a)*: A McKibben actuator's actuation region is the region where the actuator produces a tensile force at a contraction strain ($\varepsilon \leq 0$). McKibben actuators are limited physically by a maximum actuation, but the actuation region is further limited to pressures above those required to achieve a given contraction (Line IV).

• *Region II(b)*: The actuator is pressurized, but extended, which is referred to as pressurized extension. The reaction force and strain are tensile (opposite the normal actuation direction). The force is a combination of actuation and passive extension, which requires that the force be greater than that at zero strain for equivalent pressures.

• *Line III(a)*: The actuator is unpressurized and passively compressed. The Region I(a) and I(b) models, evaluated at zero pressure, must equal Line III(a) for consistency.

• *Line III(b)*: The actuator is unpressurized and passively extended. The Region II(b) model, evaluated at zero pressure, must equal Line III(b) for consistency.

• *Line IV*: The free contraction line is defined the pressure required to contract the actuator to a given strain under no load. The reaction force is zero along the line.

3 Methods

3.1 Experimental model requirements

All regions and features of the response space, except the true burst pressure, were characterized. However, characterizing a set of individual regions with experimental fits is insufficient to produce a usable response space model. Three constraints are placed on the experimental models.

1. Models are to be consistent with the anticipated response beyond tested values, in order to avoid false solutions at unexpected strains when solving system models.
2. Models in adjacent regions must be consistent at shared boundaries, such that the predicted force at the boundary is identical, regardless of which region's characterization is used to calculate it. This requirement ensures identical solutions, regardless of whether a numerical solver approaches from a higher or lower strain.
3. Models must be length independent in order to most closely mimic the material stiffnesses they are intended to replace. The validity of assuming length independence was examined (Section 4.2).

The boundary requirements for the proposed McKibben actuator response space are:

$$
\begin{aligned}
F_{I(a)}(\varepsilon_{limit}, P) &= F_{I(b)}(\varepsilon_{limit}, P),\\
F_{I(b)}(\varepsilon, P_{IV}(\varepsilon)) &= F_{II(a)}(\varepsilon, P_{IV}(\varepsilon)) = 0,\\
F_{II(a)}(\varepsilon_0, P) &= F_{II(b)}(\varepsilon_0, P),\\
F_{I(a),I(b)}(\varepsilon, P = 0) &= F_{III(a)}(\varepsilon),\\
F_{II(b)}(\varepsilon, P = 0) &= F_{III(b)}(\varepsilon).
\end{aligned}
$$

3.2 Test equipment

All force-displacement tests were conducted on a Mark-10 ESM1500 tension-compression test stand, which has a position resolution of 0.02 mm. Actuators were connected via end caps with attachment points (Figure 1(b)). The actuator's bottom, the end with the pressure inlet, was connected to the base of the test stand. The actuator's top was connected via a bracket to a 50 N load cell (model MR03-10). The maximum value of the load cell was selected based on the largest expected force, which occurs in pressurized extension (Region II(b)). The load cell had a resolution of 0.02 N and an accuracy of 0.075 N.

Correlated pressure-force-position data was gathered by reading actuator pressure from a Honeywell TruStability 30 psi (200 kPa) pressure sensor, through an Arduino. The pressure sensor has an accuracy of $\pm$0.08 psi ($\pm$0.55 kPa) and, in the test set-up, a resolution of 0.03 psi (0.2 kPa).

3.3 Test samples

Seven McKibben actuator designs were tested. Each design was fit to the same set of experimental models, in order to determine the extent to which the proposed fit forms may generalize. The variants' characterization data is further used to determine the relative effects of selected design variables. The seven designs range in tube material, tube wall thickness and actuator diameter (Table 1). The manufacturing method (Appendix A) and capping procedure were refined from accepted manufacturing techniques and were the same for each variant. All actuator sheaths were made from a commercial polyester plastic expandable sleeving (McMaster #9284K2) and were annealed to the indicated diameters.

Sample length differed necessarily between regions with tensile and compressive reactions forces. Actuators can be expected to experience local (i.e., over part of the length) compressive forces during use that would lead to buckling if experienced over longer lengths. The goal is to replace

Table 1. Actuator variations in material, inner diameter and wall thickness t.

Variant	Material	Inner Dia., Tube	t, Tube	Inner Dia., Sheath	θ
EF20-4-1	Eco-flex 00-20	4 mm	1 mm	6 mm	28.5°
EF30-4-1	Eco-flex 00-30	4 mm	1 mm	6 mm	28.5°
DS10-4-1	DragonSkin 10	4 mm	1 mm	6 mm	28.5°
EF30-2-1	Eco-flex 00-30	2 mm	1 mm	4 mm	35°
EF30-6-1	Eco-flex 00-30	6 mm	1 mm	8 mm	31°
EF30-6-0.75	Eco-flex 00-30	6 mm	0.75 mm	8 mm	31°
EF30-6-1.5	Eco-flex 00-30	6 mm	1.5 mm	9 mm	37°

simplified material models, which means the actuator model must predict the reaction force independent of length. Standard practice in material testing is to determine tensile properties on long, thin samples (e.g., dumbbell samples) and compressive properties on short, wide samples (e.g., buttons). A similar practice was adopted. Passive extension (Line III(b)), the actuation region (Region II(a)) and pressurized extension (Region II(b)) were tested with nominally 200 mm long actuators, while pressurized compression (Region I(a) and I(b)) and passive compression (Line III(a)) were tested with nominally 100 mm long actuators for all but one variant. The 2 mm inner diameter, 1 mm wall thickness actuator compression test specimens were nominally 75 mm due to their reduced critical buckling load.

Sample lengths were selected to minimize end effects, while maintaining a pure strain state. Actuator ends constrain the sheath and tube, while the rest of the length has an identical, unconstrained cross section. The EF30-4-1 variant was tested at six lengths, ranging from 75 mm to 200 mm (results in Section 4.2), which showed good agreement in the tensile results for longer samples and some sensitivity to length in the compressive results. Samples for compressive force regions were selected to have the longest length that did not buckle, while samples for tensile force regions were selected to have the longest available length.

3.4 Test procedures

Each region was characterized by displacing an unpressurized actuator to a set of pre-selected strain before pressurizing the actuator with air. Measurements were taken continuously during pressurization. The actuation region (Region II(a)) was tested in strain intervals of approximately 2% (4 mm), while the typically smaller pressurized extension region was tested in strain intervals of 0.5% (1 mm) or 1% (2 mm). Pressurized compression was tested in intervals of approximately 2%, which resulted in smaller displacements due to the shorter actuators. Actuators were pressurized manually via a syringe. Note that, except where stated, displacements were tested consecutively and without rest time between each run. Passive behavior (Line III) was tested via traditional tension and compression tests.

Five samples of each variant were tested in order to characterize Region II(a), II(b), Line IV and Line III(b), while three samples of each variant were tested to characterize Region I(a), I(b) and Line III(a). More samples were tested in the predominantly tensile regions, due to higher variations in passive extension compared to passive compression.

3.5 Error metrics

Simple fit forms are preferred over more complex ones. Though more complex fits can be more accurate, they risk overfitting. Other models of the complete uniaxial response space do not exist for comparison. This work focused on consistency at strain-pressure region boundaries and easily implemented fits. The number of samples makes it space prohibitive to show visual comparisons for all samples and regions. The fits are compared visually to the experimental data for the EF30-4-1 variant in Section 5.5, and error metrics are used to quantify fit quality elsewhere. The fit quality metrics were also used to determine coefficients through minimization. Each quality metric is based on root mean squared error (RMSE), but select regions require a weighting factor because of an unequal measurement distribution.

The simple form of RMSE is

$$\sigma_l = \sqrt{\frac{1}{N_p}\sum_{1}^{i=N_p}(F_{i,actual} - F_{i,predicted})^2}, \qquad (1)$$

where N_p is the total number of points used in the fit, and $F_{i,actual}$ and $F_{i,predicted}$ are the true and fit-predicted force, respectively, at the i^{th} point. Equation 1 was used for Line III(a), III(b) and IV, where measurements were generally equally distributed along the independent variable.

Region fit quality metrics used an area weight factor to avoid skewing the fit. Actuators were pressurized manually, which is fast, easy and cheap, but can cause different pressurization rates at different strains. This potential variance can be managed by normalizing data from each strain using a weighting metric determined by the effective pressure range at that strain. Consider a case where ten strains were tested from ε_0 to ε_{limit}, and suppose each strain has 100 points from $P_{IV}(\varepsilon)$ to P_{limit}. Without an area weighting factor, strains

closer to ε_{limit} will be overrepresented due of a higher data density (see actuation region shape in Figure 1). The error for regions σ_r was calculated with

$$\sigma_r = \sqrt{\frac{1}{W_{total}} \sum_{1}^{j=N_\varepsilon} \frac{W_j}{N_{p,j}} \sum_{1}^{i=N_{p,j}} (F_{i,j,actual} - F_{i,j,pred.})^2}. \quad (2)$$

Weights W_j were calculated from the pressure range at the j^{th} strain, which varies between region:

$$I(a) : W_j = P_{limit},$$
$$I(b) : W_j = P_{IV}(\varepsilon_j),$$
$$II(a) : W_j = P_{limit} - P_{IV}(\varepsilon_j),$$
$$II(b) : W_j = P_{limit}.$$

The summed errors in Equation 2 were divided by

$$W_{total} = \sum_{1}^{j=N_\varepsilon} W_j,$$

in order to take the error mean across strains. Note that Region I(a) and II(b) pressure ranges do not depend on strain, which is equivalent to setting $W_j = 1$ for all j and $W_{total} = N_\varepsilon$.

The fit quality is affected by the fit form and the underlying variance in the measured samples. Multiple samples were tested for each variant and the final characterizations were determined using all samples. Errors are reported for all samples as σ_{all} and for averages of individual samples as $\overline{\sigma}_{ind}$. Higher σ_{all} values are accepted for fit forms that produce low $\overline{\sigma}_{ind}$ values, because the error is caused by normal manufacturing and testing variance.

4 Sources of variance

The potential variance from hysteresis, stress relaxation and sample length are presented. McKibben actuators are heterogeneous combinations of materials (polyester plastic, silicone elastomers) with known viscoelastic properties that are convenient to model as time-, history- and length-independent materials with homogenized properties. While hysteresis and stress relaxation are understood to occur in soft actuators, the models that do not include these effects are simpler and faster to create and compute. This section evaluates the possible variance caused by factors not captured in the presented empirical models.

4.1 Hysteresis and stress relaxation

Hysteresis tests were conducted using the EF30-4-1 variant for three passive extension and three passive compression strains (2%, 4% and 6% in extension, 15%, 30% and 45% in compression). The stress relaxation of the EF30-4-1 variant was tested at the same three strains with a 15 minute hold at the designated strain. The same tests were conducted on sheath-only test samples of otherwise identical length and diameter, in order to investigate the sheath's contribution to each effect. The reaction force of the elastomeric tube alone was estimated to be <0.1 N, and it was not tested. The hysteresis and stress relaxation results are plotted in Figure 2.

The actuator relaxed to 89.7% of its initial force after 15 minutes at 45% compression, and to 80.5% at 6% extension. Hysteresis increases with strain magnitude, from a maximum difference between loading and unloading of 0.1 N at 15% compression to 0.31 N at 45%. The maximum difference between loading and unloading in extension was 2.9 N. The sheath is responsible for the majority of the actuator's compressive stiffness and hysteresis and stress relaxation in both directions. The sheath and actuator passive compression force were within 1% at 15% strain, and they differed by only 15% at 45% strain. Passively extending a sheath took 25% of the force required for an actuator, but the sheath's hysteresis was 40% that of the actuator (1.16 N vs the actuator's 2.9 N). The reaction force of the elastomeric tube is negligible at 6% strain, which suggests that actuator force is caused by interactions between the tube and sheath.

Hysteresis and stress relaxation produce the largest percent variance at high extension strains ($\varepsilon > 3\%$). Extension strains increase the sheath thread angle and place threads more directly under tension, which increases relaxation. The largest variations are expected in pressurized extension, because pressurization further increases thread tension.

4.2 Length independence

An ideal McKibben actuator, with a constant cross section for its entire length, will have the same reaction force at the same strains, regardless of length. The actuator ends, however, introduce non-uniform behavior. The response of the EF30-4-1 variant for several lengths was compared in passive compression, passive extension, the actuation region and for the free contraction line.

Six lengths were compared for passive extension, ranging from 200 mm to 75 mm (Figure 3(a)). The three shortest lengths are also compared in passive compression (Figure 3(c)). Passive extension reaction forces were similar for 150 mm to 200 mm long samples, but sample variance increased as length decreased. The most likely cause of variance is uneven clamping of the sheath to the end cap. Actuator ends are a larger fraction of the overall length in shorter actuators, and variance in the ends would have a greater effect. Shorter lengths led to visibly larger passive compression forces, but the cause is more difficult to isolate. Shorter lengths are more sensitive to actuator end stiffness, but shorter lengths are also less likely to buckle. The 125 mm long sample was observed to buckle slightly near 50% compression, but the 100 mm and 75 mm samples were not.

The free contraction lines (Line IV) for all six lengths are plotted in Figure 3(b). Strain isolines from the actuation region (Region II(a)) for 75 mm, 125 mm and 200 mm samples are compared in Figure 3(d). The free contraction line and actuation region show less effect from actuator length

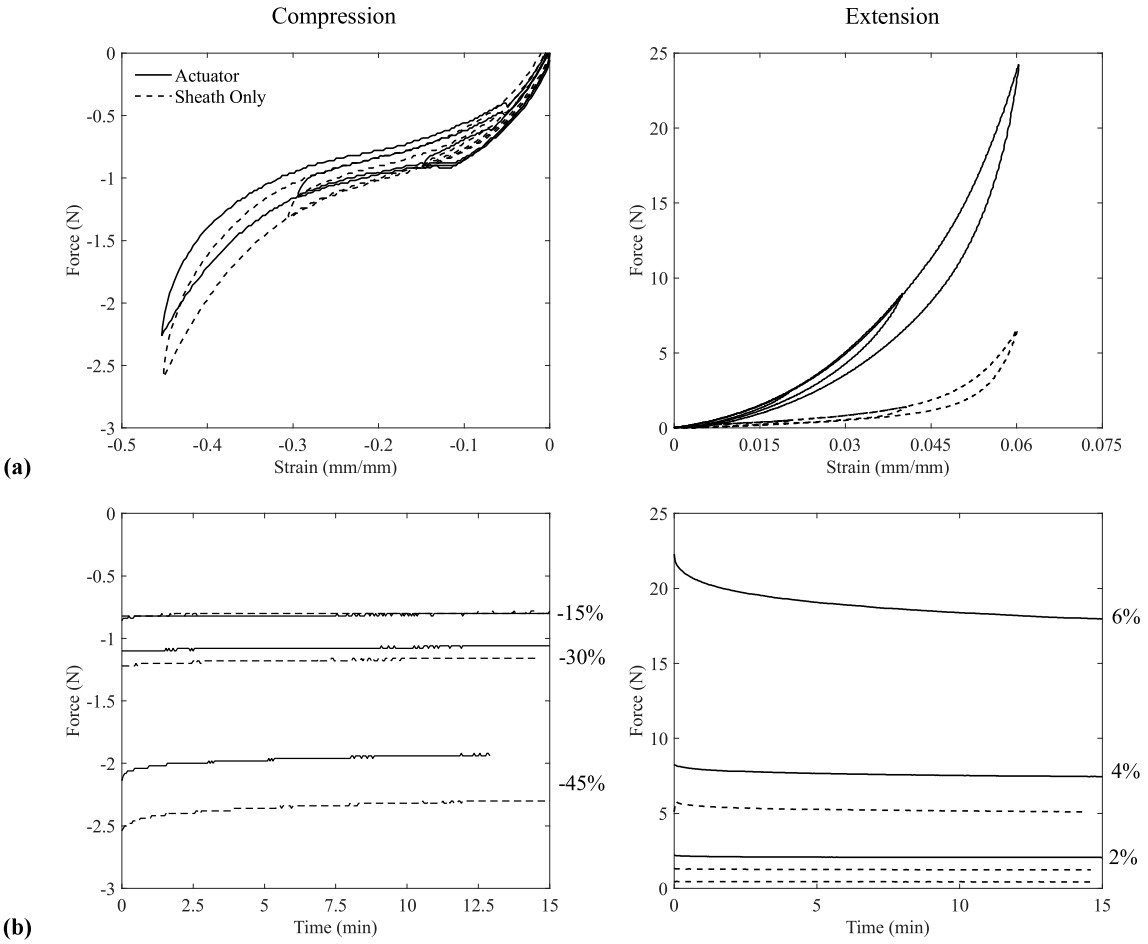

Fig. 2. (a) Hysteresis and (b) stress relaxation of an actuator and a sheath alone. Hysteresis plots show the load-unload curves up to strains of 2%, 4% and 6% in extension and 15%, 30% and 45% in compression. The strain rate in each direction was 30 mm/min. Stress relaxation results are for the same actuator at set strains of 2%, 4% and 6% in extension and 15%, 30% and 45% in compression.

than the passive results. The largest difference occurs at the shortest length. During characterization, tensile regions were tested at 200 mm in order to minimize end effects, and compressive regions were tested at the longest length with no visible buckling in order to minimize end effects to the extent possible while maintaining a pure compressive strain.

5 Characterization results

Comparative results are presented for passive extension, passive compression and the actuation region, and fit results are presented for all tested regions. Fit forms, which were developed for each region based on behavior, are presented and discussed. Physics-based models were used occasionally to guide fit form, but emphasis was placed on forms that are numerically similar to the experimental results.

Each region was fit using individual actuators to evaluate appropriateness, but final coefficients were fit using all samples for a given variant. Regions were fit in the following order, in order to reduce inaccuracy from boundary conditions in earlier regions: Line III, Line IV, Region II(a), Region II(b), Region I(b) and Region I(a).

5.1 Passive extension, passive compression and boundary strains

Passive extension and compression (Line III) are analogous to uniform tension and compression material testing, and, like many composite structures, actuators can have different stiffnesses in tension and compression. The tensile stiffness of all actuator variants was drastically higher than the compressive stiffness, and both directions were nonlinear (Figure 4). McKibben actuators are known to have limited passive extension [3], and the amount depends on weave density and the thread angle, which is related to diameter by sheath annealing (Appendix A). Passive compression is less affected by material and wall thickness because the response is sheath-dominated.

The response space boundary strains, ε_{min} and ε_{max}, were selected to be as high as possible, while minimizing the chance of damaging the actuator (Table 2). ε_{max} was selected as the strain required to generate an extension force of 12.5 N. ε_{min} was chosen as 55%, because initial tests to higher compressive strains wrinkled and permanently deformed the sheath.

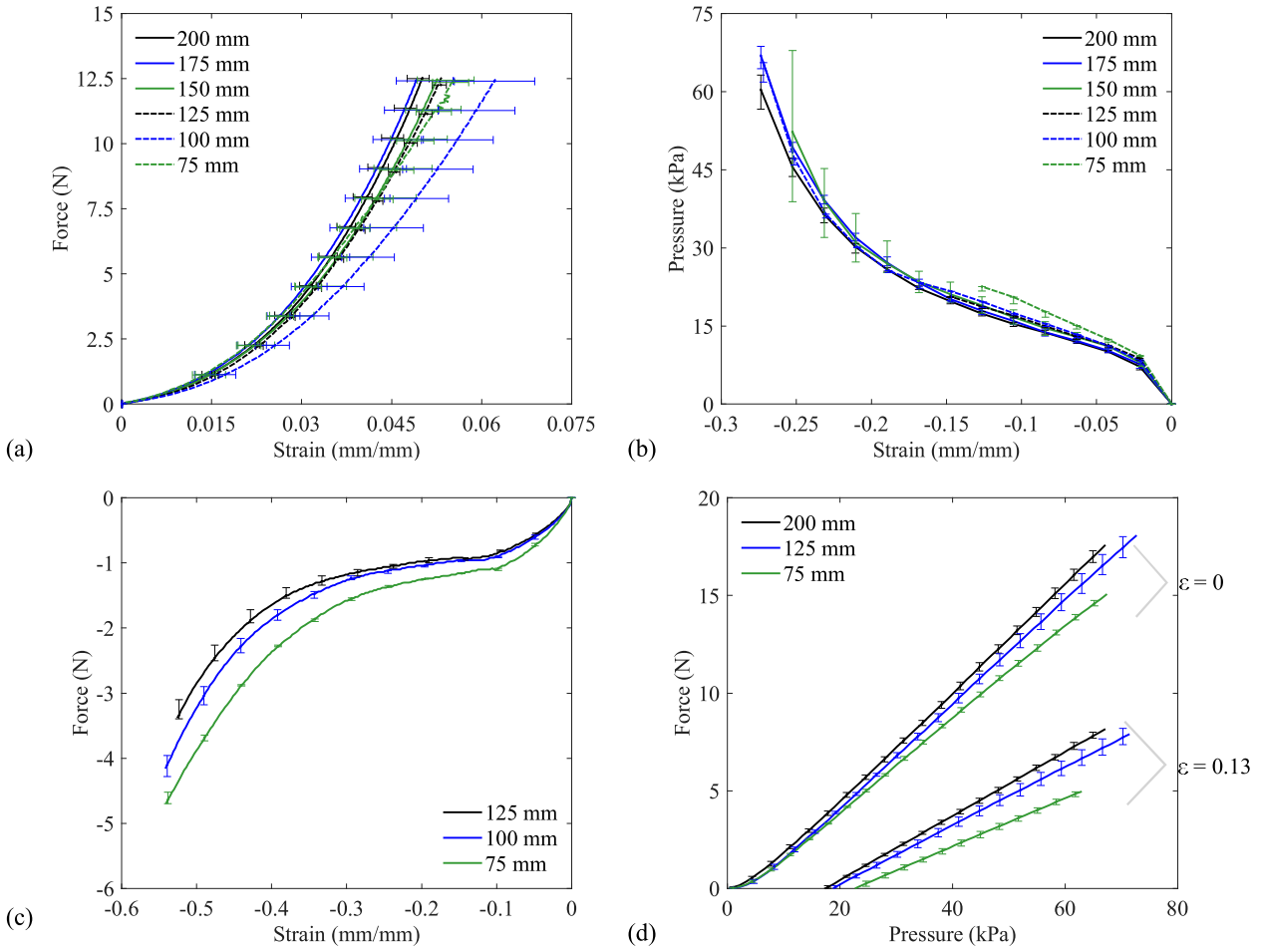

Fig. 3. Comparison EF30-4-1 responses at six lengths. Reaction force are compared for (a) passive extension, (c) passive compression and (d) actuation region (II(a)). The free contraction pressures are compared in (d). Error bars represent the range of results. A minimum of three samples were tested for each length, and five samples were tested for lengths of 150 mm, 175 mm and 200 mm.

The passive compression results were fit to

$$F_{III(a)} = k_{III(a),1}\varepsilon^4 + k_{III(a),2}\varepsilon^3 + k_{III(a),3}\varepsilon^2 + k_{III(a),4}\varepsilon \quad (3)$$

and the passive extension results were fit to

$$F_{III(b)} = k_{III(b),1}\varepsilon^3 + k_{III(b),2}\varepsilon^2 + k_{III(b),3}\varepsilon. \quad (4)$$

Table 2. Minimum and maximum strains, in mm/mm.

Variant	ε_{min}	ε_{max}
EF20-4-1	-0.55	0.052
EF30-4-1	-0.55	0.050
DS10-4-1	-0.55	0.040
EF30-2-1	-0.55	0.073
EF30-6-1	-0.55	0.10
EF30-6-0.75	-0.55	0.12
EF30-6-1.5	-0.55	0.12

The fit coefficients and qualities are provided in Table 3. The higher σ_{all} values (indicating a poorer fit quality) are driven by sample variation. The only variant not well fit ($\overline{\sigma}_{ind} > 0.5$) by the proposed forms is the thinnest wall actuator. The cause of the irregular behavior of the thinnest wall variant during extension is unknown, but the response was similar for all samples.

Lower order polynomial fits were also considered. The average error for all samples across all variants for a quadratic fit of the extension response was 0.35 N and 0.15 N for cubic fits. The average error for all samples of all variants for a cubic fit of compressive response was 0.057 N, while the selected fourth order fit had an average error of 0.041 N.

The behavior of each passive extension fit beyond the tested region was checked, and only the DS10-4-1 fit changed concavity in the extrapolated domain. All compres-

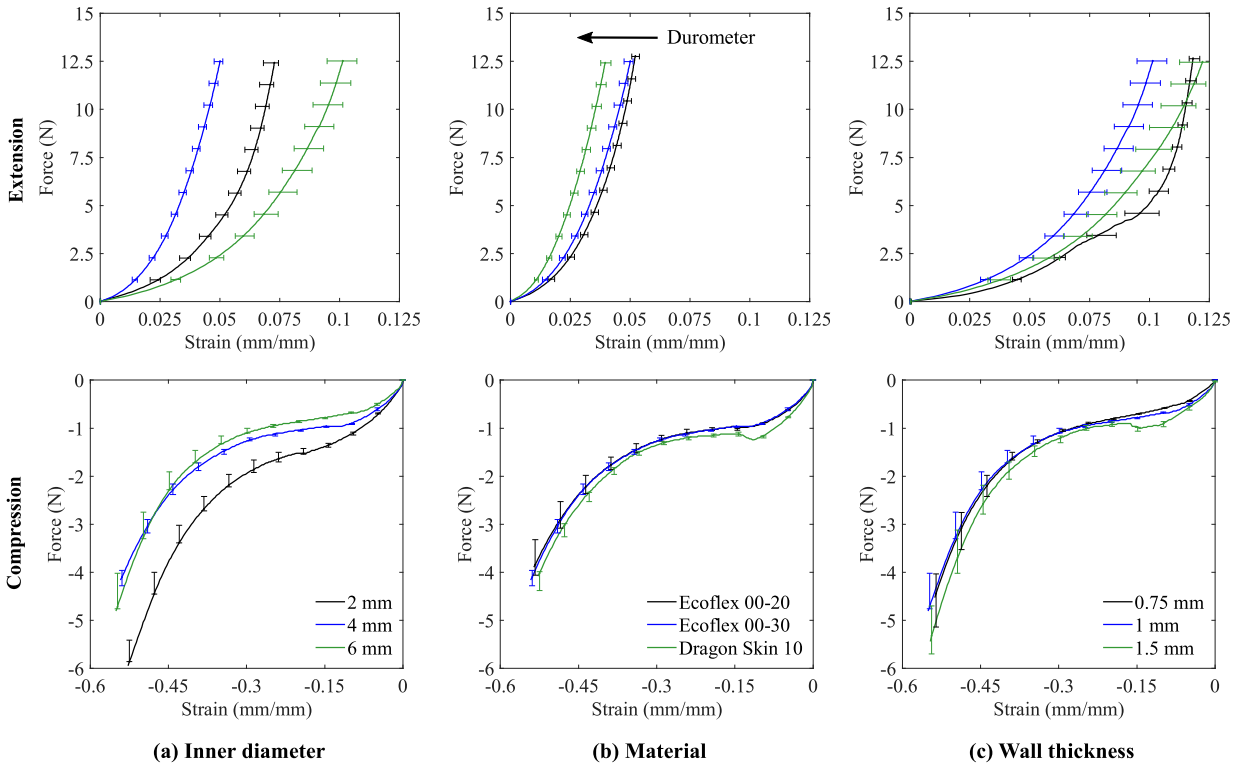

Fig. 4. Comparison of passive compression and extension response of the actuator variants in (a) inner diameter, (b) elastomer tube material and (c) tube wall thickness. Tests were conducted at a rate of 30 mm/min. The average of all samples is plotted, and the error bars represent the range of results. Passive extension results are shown in the top row, and passive compression results are shown in the bottom row.

Table 3. Passive compression (Region III(a)) and extension (Region III(b)) fit coefficients and quality metrics for all samples together σ_{all} (N), and the average fit quality for individual samples $\overline{\sigma}_{ind}$ (N).

Variant	$k_{III(a),1}$	$k_{III(a),2}$	$k_{III(a),3}$	$k_{III(a),4}$	σ_{all} ($\overline{\sigma}_{ind}$), **N**	$k_{III(b),1}$	$k_{III(b),2}$	$k_{III(b),3}$	σ_{all} ($\overline{\sigma}_{ind}$),**N**
EF20-4-1	95.8	175	81.5	15.5	0.12 (0.041)	67900	82.4	47.6	0.33 (0.063)
EF30-4-1	70.7	151	74.2	14.7	0.071 (0.037)	31500	2750	28.3	0.35 (0.024)
DS10-4-1	166	263	117	20.2	0.085 (0.052)	-31500	8550	13.1	0.47 (0.025)
EF30-2-1	73.0	175	85.2	18.4	0.12 (0.028)	37600	-1400	59.3	0.44 (0.20)
EF30-6-1	-40.8	44.4	38.6	10.2	0.14 (0.045)	6040	325	18.3	0.57 (0.093)
EF30-6-0.75	-60.1	13.6	24.4	8.08	0.16 (0.039)	9490	-770	41.5	0.63 (0.58)
EF30-6-1.5	11.2	118	68.3	14.0	0.19 (0.050)	3920	155	17.8	0.54 (0.060)

sive fits maintained the same concavity up to a strain of -0.8, and the EF30-4-1, EF30-2-1, EF30-6-1, EF30-6-0.075 and EF30-6-1.5 variants maintained concavity past -0.9 (note that -1.0 is equivalent to 100% compression, or perfectly flat).

5.2 Actuation region and free contraction line

The actuation region (Region II(a)) is bounded on the top by a user selected maximum pressure and on left and bottom by the free contraction line (Line IV). An ideal McKibben actuator, with no losses to the sheath or bladder, can contract until the maximum volume is reached, which nominally occurs when the sheath angle reaches 54.7°, measured from the helix axis [3]. However, energy is lost to the tube and sheath, which limits the amount of contraction possible at a given pressure. The free contraction line represents the amount of pressure it takes to reach a given contraction strain with no load on the actuator.

The actuation region model is based on observation of the test result form and the virtual work model of ideal McKibben actuators developed in prior studies [3], [17]:

$$F_{ideal} = \frac{\pi D_0^2 P}{4}(3\sin^2\theta - 1), \tag{5}$$

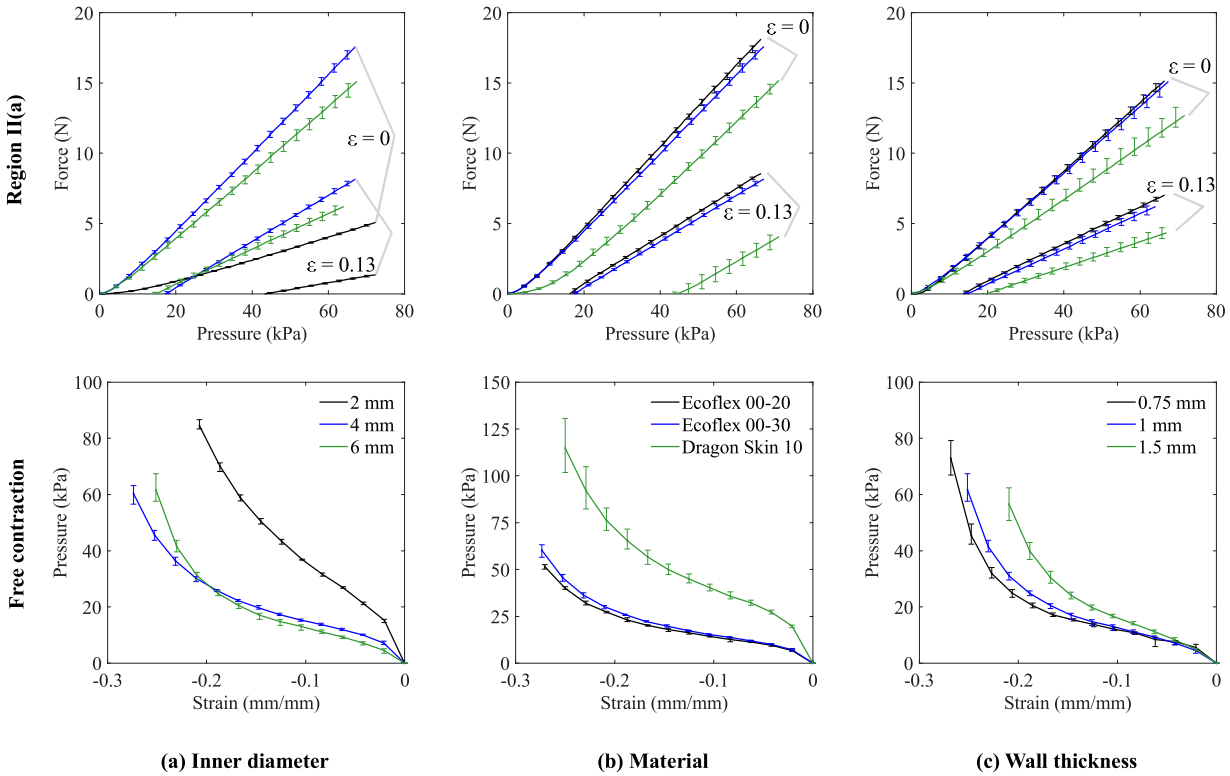

Fig. 5. Comparison of the free contraction line and actuation region behavior for the tested actuator variants. Two sample strain isolines are plotted for each actuation region comparison. The plotted line indicates the average response for each variant, while the error bars show the response range across all five samples. (a) Comparison of varying actuator diameter. (b) Comparison of varying elastomer tube material. (c) Comparison of varying tube wall thickness.

where $\frac{\pi D_0^2}{4}$ is a geometric factor, P is actuator pressure and θ is the thread angle. It can be shown that $\sin\theta \propto \varepsilon$. The measured reaction forces were linearly dependent on pressure for most variants (Figure 5), but nonlinearly dependent on strain, which matches the existing physics-based models. The reaction force was modeled as

$$F_{II(a)}(\varepsilon, P) = k_{II(a),1}(k_{II(a),2} + \varepsilon)^2 (P - P_{IV}(\varepsilon)), \qquad (6)$$

where P is the actuator gauge pressure and P_{IV} is the pressure required to freely contract the actuator to strain ε. P_{IV} acts as a correction factor on the linear pressure term, and is modeled as

$$P_{IV} = k_{IV,1}\varepsilon^3 + k_{IV,2}\varepsilon^2 + k_{IV,3}\varepsilon. \qquad (7)$$

Third and forth order polynomial fits of the free contraction line were investigated. The fit quality was calculated using Equation 1. Third order fits had, across all samples of all variants, an average error of 1.42 kPa, while fourth order fits had an error of 1.00 kPa. Maximum pressures ranged from 68.9 kPa (10 psi) to 110 kPa (16 psi), which means the improvement, as a percentage of the maximum pressure, is 0.6% and 0.4%, respectively. A third order fit was selected as the simplest fit beyond which returns diminish. The fit coefficients and qualities are provided in Table 5.

Table 4. Actuation region (Region II(a)) fits coefficients and quality (N).

Variant	$k_{II(a),1}$	$k_{II(a),2}$	σ_{all} ($\bar{\sigma}_{ind}$),N
EF20-4-1	1.03	0.528	0.44 (0.43)
EF30-4-1	0.906	0.548	0.40 (0.39)
DS10-4-1	0.651	0.601	1.4 (1.1)
EF30-2-1	2.35E-5	-52.2	0.29 (0.25)
EF30-6-1	1.09	0.462	0.36 (0.32)
EF30-6-0.75	1.15	0.460	0.43 (0.42)
EF30-6-1.5	0.946	0.438	0.36 (0.26)

The free contraction line data extracted from compression samples, gathered during pressurized compression testing, was not used to in Line IV fits. The last column in Table 5, σ_c, gives the quality of the presented coefficients for the compression sample data. Mismatches are expected due to end effects and sample variance, but the extent of the mismatches are an indication of the deviations likely to be introduced by imposing continuity between Region I(b) and II(a).

The fit coefficients and quality metrics for Region II(a)

Table 5. Free contraction (Line IV) fit coefficients and quality measures (kPa). σ_c is the fit quality for data collected on compression samples.

Variant	$k_{IV,1}$	$k_{IV,2}$	$k_{IV,3}$	σ_{all} ($\overline{\sigma}_{ind}$)	σ_c
EF20-4-1	-7620	-2530	-325	1.4 (1.1)	2.9
EF30-4-1	-7430	-2400	-322	1.0 (0.84)	2.1
DS10-4-1	-16100	-5400	-791	5.0 (1.9)	17
EF30-2-1	-16400	-4610	-667	1.3 (1.2)	7.7
EF30-6-1	-10100	-2810	-301	1.8 (1.5)	3.3
EF30-6-0.75	-11400	-3430	-347	2.8 (2.5)	5.7
EF30-6-1.5	-14000	-3230	-336	1.9 (1.2)	5.0

are given in Table 4. All fits use the free contraction line coefficients from Table 5. Improving free contraction line fits did not necessarily provide equivalent improvements in the actuation region fit. For instance, fitting P_{IV} to a fourth degree polynomial for variant EF30-6-1 improved $\sigma_{all,IV}$ from 2.19 kPa^2 to 0.74 kPa^2, but only improved $\sigma_{all,II(a)}$ from 0.13 N^2 to 0.12 N^2. Poorer fits occurred in actuators with nonlinear initial pressure responses (see Figure 5(b), Dragon Skin 10 at $\varepsilon = 0$), which cannot be matched by the model.

Reaction forces for two strain isolines and the free contraction line are compared in Figure 5. Eco-flex 00-20 and Eco-flex 00-30 show nearly identical responses, as do variants with wall thicknesses of 0.75 mm and 1 mm. The response similarity suggests there is a point of diminishing returns on softening tubes to reduce lost energy. Dragon Skin 10 requires more than double the pressure to contract, which is not compensated for by the maximum achieved force.

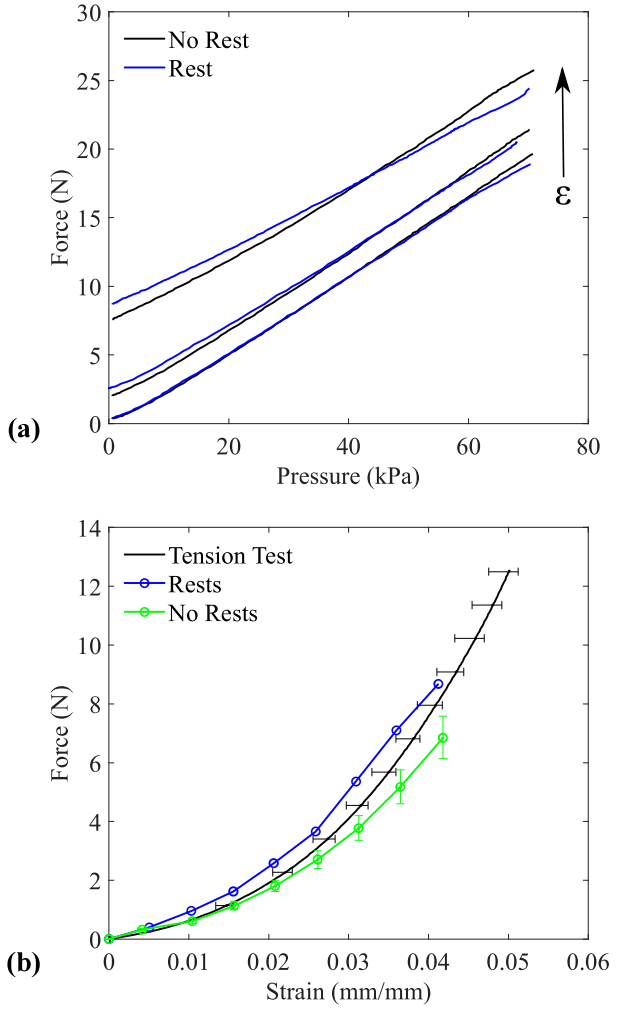

Fig. 6. Comparison of EF30-4-1 pressurized extension response for a sample rested 30 minutes between each tested strain and the same sample tested without rests. (a) Strain isolines for rested and unrested results. (b) Comparison of passive extension response for for all EF30-4-1 tensile test data and passive extension data extracted from pressurized extension testing.

5.3 Pressurized extension

Pressurized extension goes from zero strain to ε_{max}, but the region is not limited by a free contraction line. The tensile reaction force is a combination of the actuator force and the passive extension force, which acts as a pretension for any given strain isoline (Figure 6). The actuation region experimental model was modified to account for this addition and to incorporate nonlinearity into the pressure response:

$$F_{II(b)} = F_{III(b)}(\varepsilon) + k_{II(b),1}(k_{II(b),B} + k_{II(b),2}\varepsilon)^2 P^{(1+k_{II(b),3}\varepsilon)}. \quad (8)$$

Evaluating Equation 8 at $P = 0$ yields the passive extension force $F_{III(b)}$, which satisfies the Region III(b) constraint. The left boundary constraint is derived by evaluating Equation 6 (Region II(a)) and Equation 8 at $\varepsilon = 0$. The constraint is

$$k_{II(b),B} = \frac{\sqrt{k_{II(a),1} k_{II(a),2}^2}}{k_{II(b),1}}. \quad (9)$$

Note that the form of the pressure power law, $P^{1+k_{II(b),3}\varepsilon}$, added for nonlinearity, reduces to a linear pressure term, P, at $\varepsilon = 0$.

Pressurized extension produces the highest reaction forces, and is the region subject to the most stress relaxation and hysteresis. Samples were tested sequentially with no rests, due to the impracticality of testing all samples with a rest between each strain isoline. One EF30-4-1 sample was tested with a 30 minute rest between each strain to investigate variance (Figure 6(a)). The passive extension force was extracted from the pressurized extension results at $P = 0$ (Figure 6(b). The unrested test passive extension force was lower than the rested test and the tensile test, as expected. The rested test reaction force approaches the unrested test as pressure increases, but the initial difference lowers fit quality when the Region III(b) boundary condition is applied.

The pressurized extension region was fit three times in

Table 6. Pressurized extension (Region II(b)) fit qualities (N).

Variant	Unconst. $\overline{\sigma}_{ind}$, N	Const. $\overline{\sigma}_{ind}$, N	All Data σ_{all}, N
EF20-4-1	0.26	0.58	0.64
EF30-4-1	0.25	0.47	0.48
DS10-4-1	0.59	1.03	1.2
EF30-2-1	0.14	0.24	0.22
EF30-6-1	0.23	0.76	1.2
EF30-6-0.75	0.26	0.62	0.63
EF30-6-1.5	0.18	0.26	0.62

Table 7. Pressurized extension (Region II(b)) fit coefficients.

Variant	$k_{II(b),1}$	$k_{II(b),2}$	$k_{II(b),3}$
EF20-4-1	1.95	-3.27	4.07
EF30-4-1	1.92	-3.76	5.32
DS10-4-1	1.88	-3.38	4.51
EF30-2-1	1.09	-2.44	6.60
EF30-6-1	1.45	-2.03	3.18
EF30-6-0.75	1.15	-1.44	2.10
EF30-6-1.5	1.00	-1.17	2.07

order to demonstrate the effect of sample variance, exacerbated by stress relaxation and hysteresis, and boundary conditions on fit quality. Fit quality was calculated using Equation 2. The *unconstrained* column in Table 6 provides the average fit quality of individual fits with no boundary conditions. The *constrained* column also presents individual fits, but uses $F_{III(b)}$ from Table 3 and enforces Equation 9. The third column, *All Data*, enforces the same boundary conditions and fits to all samples. Boundary constraints and sample variance are the largest drivers of poorer fits, and individual samples are well fit for five of the seven variants. Fit coefficients are given in Table 7.

5.4 Pressurized compression

Pressurized compression (Region I) encompasses the largest range in behavior and the most complex mechanics. Region I is split into Region I(a) and I(b) at ε_{limit}, which is the strain at which an actuator pressurized to P_{limit} produces zero force. Region I(b) lies under the free contraction line, and the behavior transitions from passive stiffness to actuation. Region I(a) encompasses the rest of the strains, stretching left to ε_{min}. The actuator behaves like a McKibben actuator from ε_{limit} to ε_{crit}, and the strain isolines have a positive slope. The actuator reaches the true critical strain ε_{crit}, and the slope of the strain isoline becomes negative. Past ε_{crit}, the actuator behaves like an extending actuator (Figure 7(a)).

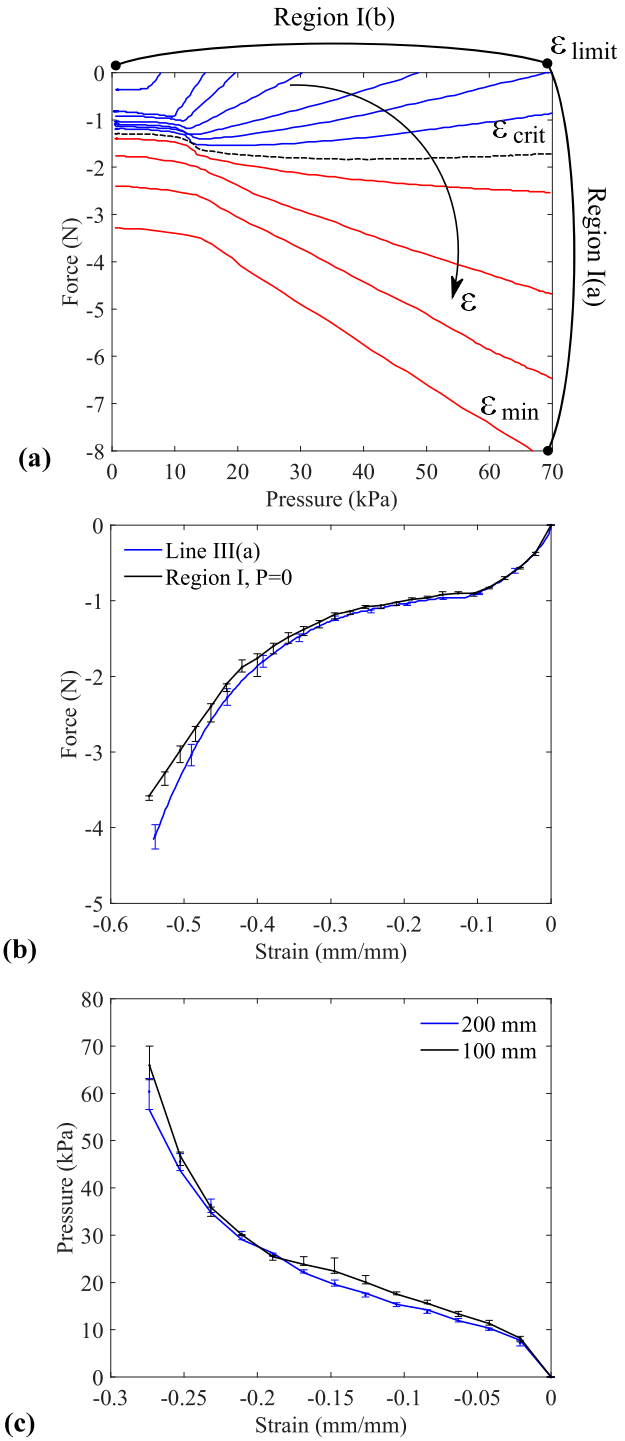

Fig. 7. EF30-4-1 actuator behavior in pressurized compression. (a) Strain isolines showing the actuator change from a contracting mode (blue) to an extending mode (red) as the compressive strain increases. (b) Comparison of passive compression behavior when directly tested vs extracted from pressurized compression test data. (c) Comparison of the free contraction line (Line IV) for a 100 mm long sample and a 200 mm long sample.

Region I(b) borders the actuation region on the free contraction line (Line IV), and must reach zero force along that line. At $P = 0$, Region I(b) must equal passive compression

(Region III(a)). Region I(b) is modeled by

$$F_{I(b)} = F_{III(a)}(\varepsilon), \quad \{P : 0 \leq P \leq P_{crit}\}, \tag{10}$$

$$F_{I(b)} = F_{III(a)}(\varepsilon) + k_{I(b),1}(k_{I(b),2} + \varepsilon)^2 (P - P_{crit}), \quad \{P : P \geq P_{crit}\}. \tag{11}$$

The critical pressure, P_{crit}, represents the pressure at which the inflating tube contacts the sheath. The Line III(a) and Line IV boundary requirements defines P_{crit}, which can be found by evaluating Equation 11 at the free contraction line (Line IV). The force must be zero at the free contraction line, which gives the following boundary condition:

$$P_{crit} = \frac{F_{III(a)}}{k_{I(b),1}(k_{I(b),2} + \varepsilon)^2} + P_{IV}(\varepsilon). \tag{12}$$

Evaluating Equation 11 at $P = 0$ yields the Line III(a), which satisfies the passive compression boundary condition.

Region I(a) is bounded by passive compression and the border with Region I(b) at ε_{limit}. The proposed model divides the region at ε_{crit}, which is defined as the location at which the force-pressure slope is zero beyond P_{crit}. Regardless of strain, the critical pressure is calculated by evaluating Equation 12 at ε_{limit}. The reaction force below P_{crit} is modeled by Equation 10. The force above P_{crit} is modeled as

$$F_{I(a)} = F_{III(a)}(\varepsilon) + k_{I(a),B}(-\varepsilon_{crit} + \varepsilon)^2 (P - P_{crit}) \tag{13}$$

for $\{\varepsilon : \varepsilon_{limit} \geq \varepsilon \leq \varepsilon_{crit}\}$. The model form guarantees a zero slope at the critical strain. The negative slope region follows a similar form to guarantee consistency at the boundary:

$$F_{I(a)} = F_{III(a)}(\varepsilon) - k_{I(b),1}(-\varepsilon_{crit} + \varepsilon)^2 (P - P_{crit}). \tag{14}$$

The boundary condition between Region I(a) and I(b) defines the fit coefficient as

$$k_{I(a),B} = \frac{k_{I(b),1}(k_{I(b),2} + \varepsilon_{limit})^2}{(-\varepsilon_{crit} + \varepsilon_{limit})^2}. \tag{15}$$

The limit strain was found by evaluating the Line IV fits (Table 5) at P_{limit}. The critical strain was determined by interpolating strain isoline slopes to estimate the zero slope strain.

The fit qualities and coefficients are given in Table 8. Fit quality was calculated with Equation 2. The boundary conditions limited fit quality, as they did in pressurized extension, but the greater limitation was the complexity of the mechanics. The reaction force at the edges of Region I is well-defined by linear pressure responses near P_{IV} or P_{limit}, and zero slope lines equal to the passive compression force at $P = 0$ kPa (Figure 7(a)). The center of Region I, however, is determined by interactions between the sheath and the wrinkled or folded tube, as the tube inflates. Folds likely affect inflation, but the extent of effect is different between an actuator with a 0.75 mm thick wall, made from Eco-flex 00-30, and one with a 1 mm thick Dragon Skin wall. The characterization assumes path independent, sheath-dominated behavior. Path-dependent models, while potentially more accurate, are also much more complex. The Region I model forms were selected because they capture the dominant behaviors and meet the boundary conditions.

The fit coefficients from Table 3 were used for the Line III(a) boundary. The passive compression data extracted from the pressurized compression test is compared to the Line III(a) test for one variant in Figure 7(b). Line III(a) was tested at a rate of 30 mm/min (total test time of 1.8 min), while pressurized compression testing took approximately 30 minutes to test all strains. The difference between the two lines is likely caused by stress relaxation, and is a possible source of variance at high compressive strains. The fits in Table 5 were used for the free contraction line, for consistency with Region II(a), which is another potential source of variance. Shorter samples are required for compression, but the larger end effects caused RMSEs of at least 2 kPa when the free contraction coefficients from tensile samples were evaluated with data from compression samples. The difference between the free contraction for one 200 mm and

Table 8. Pressurized compression (Region I(a), I(b)) fit coefficients and qualities, measured in N.

Variant	$k_{I(a),1}$	ε_{crit}	σ_{all} ($\overline{\sigma}_{ind}$), N	$k_{I(b),1}$	$k_{I(b),2}$	ε_{limit}	σ_{all} ($\overline{\sigma}_{ind}$), N
EF20-4-1	3.33	-0.326	0.69 (0.64)	2.58	0.396	-0.281	0.14 (0.092)
EF30-4-1	2.77	-0.321	0.71 (0.69)	2.28	0.393	-0.278	0.11 (0.094)
DS10-4-1	4.02	-0.331	1.59 (2.02)	1.60	0.375	-0.274	0.37 (0.25)
EF30-2-1	0.045	-0.292	0.37 (0.20)	0.348	0.509	-0.157	0.19 (0.036)
EF30-6-1	1.55	-0.278	0.80 (1.1)	4.39	0.317	-0.255	0.20 (0.15)
EF30-6-0.75	2.56	-0.288	0.88 (0.77)	3.70	0.341	-0.259	0.17 (0.09)
EF30-6-1.5	1.72	-0.240	0.96 (0.87)	3.32	0.30	-0.208	0.17 (0.08)

one 100 mm long EF30-4-1 actuator is shown in Figure 7(c).

At the far left edge of Region I(a), the compressed actuator is susceptible to a type of buckle. The compressive reaction force increases with strain and pressure, and eventually reaches a strain where the lower energy state is extended and bowed left or right (Figure 1(b), ε_{min}). This condition is not necessarily a failure, but may be undesirable.

5.5 EF30-4-1 response model

Figure 8 compares the fits for all regions and features of the EF30-4-1 variant to the experimental data. The complete model uses 18 fitted coefficients (ε_{crit} and ε_{limit} are calculated directly, not fit through minimization), but each region averages three coefficients. The ratio of coefficients to data points in most regions is on the order of 1:100 or 1:1000. The feature most susceptible to potential overfitting is Line IV, which has the fewest points. However, visual comparisons, like the one in Figure 8(b), do not show evidence of overfitting when fit with a cubic polynomial.

Figure 9 shows the full EF30-4-1 response model, with the tensile regions shown in red and the compressive regions shown in blue. The boundary between tensile and compressive regions is, by definition, the free contraction line.

6 Conclusion

This article considered the complete strain-pressure response space of a McKibben actuator, as a representative of a larger group of fluid driven soft actuators. Fluid driven soft actuators have been well studied as primary movers, but in soft systems are also used as support structures. Complex loadings, such as those that may be encountered in unstructured environments, are likely to push soft actuators out of the actuation region and into states of passive or pressurized extension and compression.

A McKibben actuator strain-pressure space was divided into regions, which were selected based on their core behavior (e.g., during actuation inflation expands the sheath to produce contraction with a tensile reaction force). Grouping like behavior allowed the development of simple, experimental reaction force models for each region. Fit coefficients and qualities were presented for seven variants. The proposed fits were more successful for actuators made from low durometers (e.g., Eco-flex 00-30), with relatively thin walls, than actuators made from stiffer elastomers (e.g., Dragonskin 10). Regions were fit in the following order to reduce inaccuracy from boundary conditions in earlier regions: Region II(a), Line IV, Line III, Region II(b), Region I(b) and Region I(a). The largest error occurred at high compression strains and pressures, due to tube buckling and boundary constraints from other regions. More complex fitting techniques, such as a surface fit or a machine learning, may produce for accurate models for pressurized compression, but any higher order model will be more susceptible to overfitting. The presented results reinforce the complexity of soft actuator mechanics, and emphasize additionally the role of sample variance, hys-

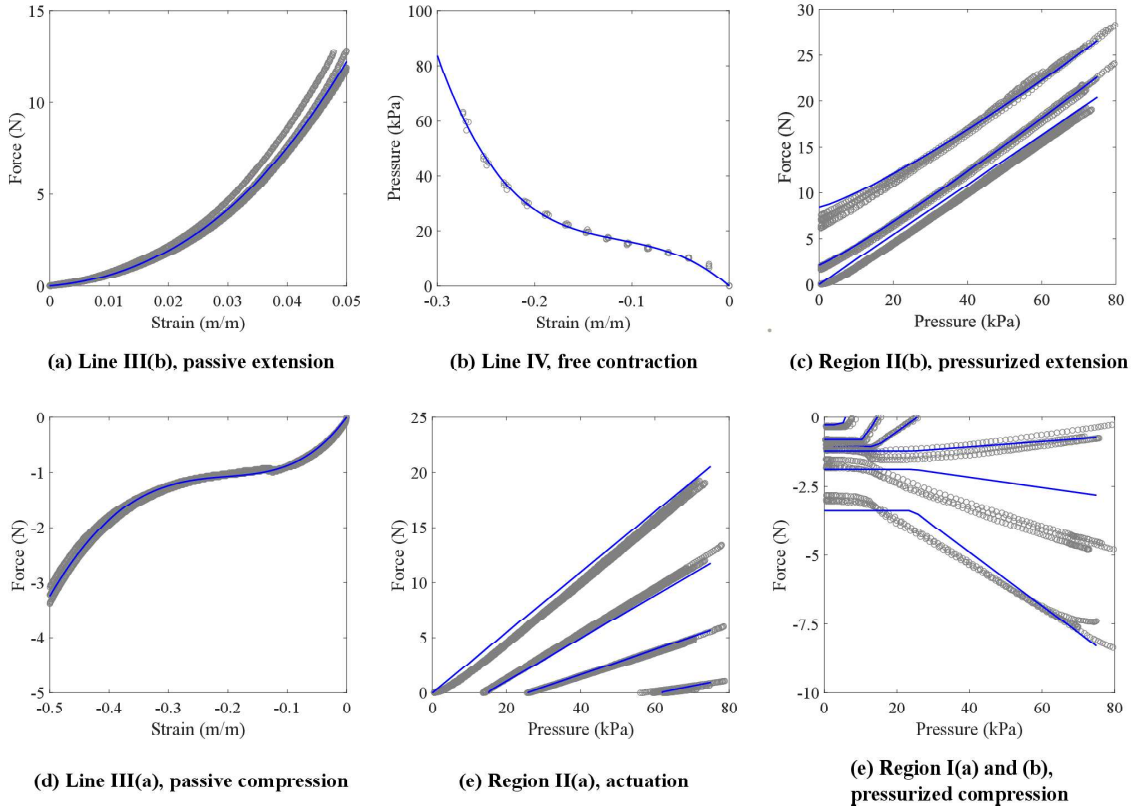

(a) Line III(b), passive extension **(b) Line IV, free contraction** **(c) Region II(b), pressurized extension**

(d) Line III(a), passive compression **(e) Region II(a), actuation** **(e) Region I(a) and (b), pressurized compression**

Fig. 8. Comparison of the experimental results (gray dots) and fitted model (blue lines) for each region and feature of the EF30-4-1 variant.

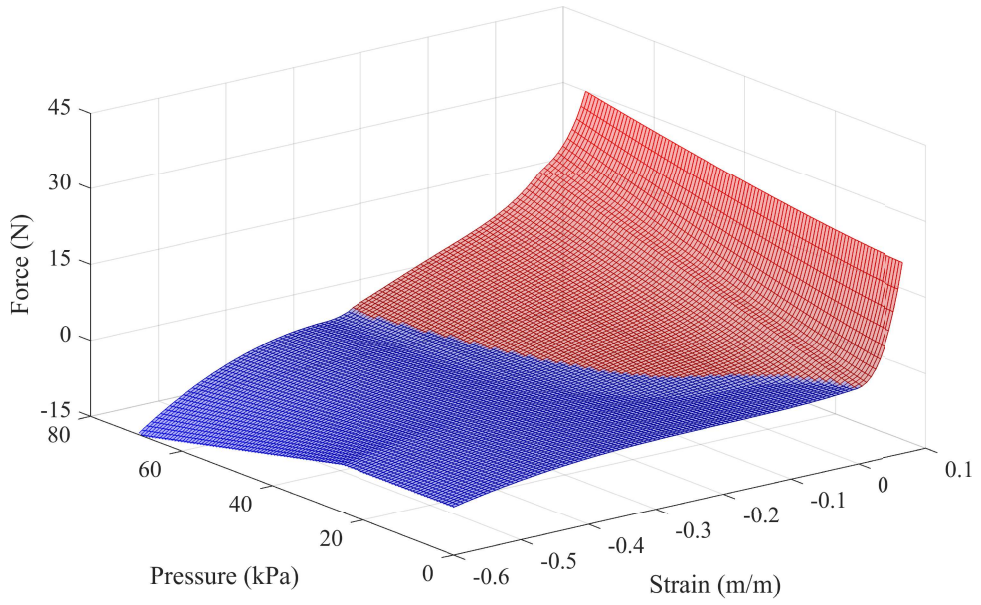

Fig. 9. The EF30-4-1 response model. Tensile regions are shown in red, while compressive regions are shown in blue.

teresis and stress relaxation as a source of uncertainty.

While McKibben actuators were the focus of this work, they are not the only the actuator that may be operated outside of their actuation region. Extending actuators, whether they use a braided sheath or reinforcing rings, may be compressed or pulled beyond their maximum stroke. The region shapes of other actuators' response spaces will vary, and the specific fits may not apply. However, actuators are expected to share certain characteristics, such as a free actuation line, and models will share common requirements, most notably that boundaries between regions be consistent.

The presented experimental models are intended to improve soft roboticist's ability to model, predict and understand more complex soft structures built from constituent actuators. Soft arms, most commonly constructed from parallel combinations of contracting or extending actuators, are particularly targeted. The experimental models can replace more simplistic force expressions in arm models, including constant curvature, beam or rod models. The technique presented is a foundation for building holistic and precise soft actuators models, and it can be extended to other actuators for use in grippers or locomoting soft robots.

Acknowledgements

This work was supported in part by the National Science Foundation (award IIS-1734627).

References

[1] Galloway, K. C., Becker, K. P., Phillips, B., Kirby, J., Licht, S., Tchernov, D., Wood, R. J., and Gruber, D. F., 2016. "Soft robotic grippers for biological sampling on deep reefs". *Soft Robotics,* **3**(1).

[2] Hawkes, E., Blumenschein, L., Greer, J., and Okamura, A., 2017. "A soft robot that navigates its environment through growth". *Science Robotics,* **2**.

[3] Chou, C., and Hannaford, B., 1996. "Measurement and modeling of mckibben pneumatic artificial muscles". *IEEE Transactions on Robotics and Automation,* **12**(1), pp. 90–102.

[4] Doumit, M., Fahim, A., and Munro, M., 2009. "Analytical modeling and experimental validation of the braided pneumatic muscle". *IEEE Transactions on Robotics,* **25**(6), pp. 1282–1291.

[5] Tondu, B., 2012. "Modelling of the mckibben artificial muscle: A review". *Journal of Intelligent Material Systems and Structures,* **23**(3), pp. 225–253.

[6] Walker, I., Dawson, D., Flash, T., Grasso, F., Hanlon, R., Hochner, B., Kier, W., Pagano, C., Rahn, C., and Zhang, Q., 2005. "Continuum robot arms inspired by cephalopods". *Proceedings SPIE Conference on Unmanned Ground Vehicle Technology VII*, pp. 303–314.

[7] Ansari, Y., Manti, M., Falotico, E., Cianchetti, M., and Laschi, C., 2018. "Multiobjective optimization for stiffness and position control in a soft robot arm module". *IEEE Robotics and Automation Letters,* **3**.

[8] Guglielmino, E., Tsagarakis, N., and Caldwell, D., 2010. "An octopus anatomy-inspired robotic arm". *IEEE/RSJ International Conference on Intelligent Robots and Systems (IROS 2010)*.

[9] Case, J., Booth, J., Shah, D., Yuen, M., and Kramer-Bottiglio, R., 2018. "State and stiffness estimation using robotic fabrics". *IEEE RoboSoft 2018*.

[10] Trivedi, D., Lotfi, A., and Rahn, C. D., 2008. "Geometrically exact models for soft robotic manipulators". *IEEE Transactions on Robotics,* **24**(4), pp. 773–780.

[11] Connolly, F., Walsh, C., and Bertoldi, K., 2017. "Automatic design of fiber-reinforced soft actuators for trajectory matching". *Proceedings of the National*

Academy of Sciences of the United States of America (PNAS), **114**(1), pp. 51–56.

[12] Shapiro, Y., Gabor, K., and Wolf, A., 2015. "Modeling a hyperflexible planar bending actuator as an inextensible euler-bernoulli beam for use in flexible robots". *Soft Robotics,* **2**(2).

[13] Giannaccini, M., Xiang, C., Atyabi, A., Theodoridis, T., Nefti-Meziani, S., and Davis, S., 2018. "Novel design of a soft lightweight pneumatic continuum robot arm with decoupled variable stiffness and positioning". *Soft Robotics,* **5**(1).

[14] Olson, G., Chow, S., Nicolai, A., Branyan, C., Hollinger, G., and Mengüç, Y., 2019. "A generalizable equilibrium model for bending soft arms with longitudinal actuators". *The International Journal of Robotics Research,* **0**(0).

[15] Pillsbury, T. E., Guan, Q., and Wereley, N. M., 2016. "Comparison of contractile and extensile pneumatic artificial muscles". *IEEE/ASME International Conference on Advanced Intelligent Mechatronics, AIM*, pp. 94–99.

[16] Koizumi, S., Kurumaya, S., Nabae, H., Endo, G., and Suzumori, K., 2018. "Braiding thin mckibben muscles to enhance their contracting abilities". *IEEE Robotics and Automation Letters,* **3**(4), pp. 3240–3246.

[17] Gaylord, R., Jul. 22, 1958. Fluid actuated motor system and stroking device. U.S. Patent 2 238 058.

[18] Schulte, H., 1961. "The characteristics of the mckibben artificial muscle". In *The Application of External Power in Prosthetics and Orthotics*. National Academy of Sciences.

[19] Tsagarakis, N., and Caldwell, D., 2000. "Improved modelling and assessment of pneumatic muscle actuators". *IEEE International Conference on Robotics and Automation (ICRA 2000),* **4**, pp. 3641–3646.

[20] Antonelli, M., Zobel, P. B., Durante, F., and Raparelli, T., 2017. "Numerical modelling and experimental validation of a mckibben pneumatic muscle actuator". *Journal of Intelligent Material Systems and Structures,* **28**(19), pp. 2737–2748.

[21] Case, J. C., Yuen, M. C., Jacobs, J., and Kramer-Bottiglio, R., 2019. "Robotic skins that learn to control passive structures". *IEEE Robotics and Automation Letters,* **4**(3), pp. 2485–2492.

[22] Meller, M. A., Bryant, M., and Garcia, E., 2014. "Reconsidering the mckibben muscle: Energetics, operating fluid, and bladder material". *Journal of Intelligent Material Systems and Structures,* **25**(18), pp. 2276–2293.

[23] Al-Ibadi, A., Nefti-Meziani, S., and Davis, S., 2016. "Valuable experimental model of contraction pneumatic muscle actuator". *International Conference on Methods and Models in Automation and Robotics (MMAR 2016)*, pp. 744–749.

A Actuator manufacturing

Each elastomeric tube was manufactured with the following procedure.

1. Clean the mold halves, mandrel and funnel with isopropyl alcohol and apply release agent. Allow five minutes for the release agent to dry (Figure 10(a)).
2. Assemble the mold and place it in the degassing chamber (Figure 10(b)).
3. Mix silicone (e.g., Eco-flex 00-30) Part A and B using a Thinky ARE-310 mixer.
4. Pour the mixed silicone into the funnel and immediately begin degassing. Degas for 2 minutes and 30 seconds.
5. Remove the mold from the degassing chamber and allow silicone to fall to the bottom by gravity. As needed, shake the mold on an orbital shaker table at 80-100 rpm.
6. When the silicone reaches the bottom, block the lower vent hole with clay.
7. Allow the silicone to cure and demold.

The sheaths were annealed to the desired configuration prior to actuator assembly. Sheaths for EF30-2-1 were initially nominally 1/8" in diameter. Sheaths for all other variants were initially nominally 1/4" in diameters.

The annealing procedure was:

1. Slide the sheath onto a rod with the same diameter as the final desired inner diameter of the sheath.
2. Trim the sheath to the length of the rod and place the rod and sheath in the oven.
3. Heat to 140 C at a rate of no more than 20 C per hour.
4. Dwell at 140 C for one hour.
5. Cool from 140 C to room temperature at a rate of no more than 10 C per hour.
6. Remove the annealed sheath from rod.

The completed sheath and tube were cut to the desired length and then assembled to the caps with cable ties (Figure 10(c) and (d)).

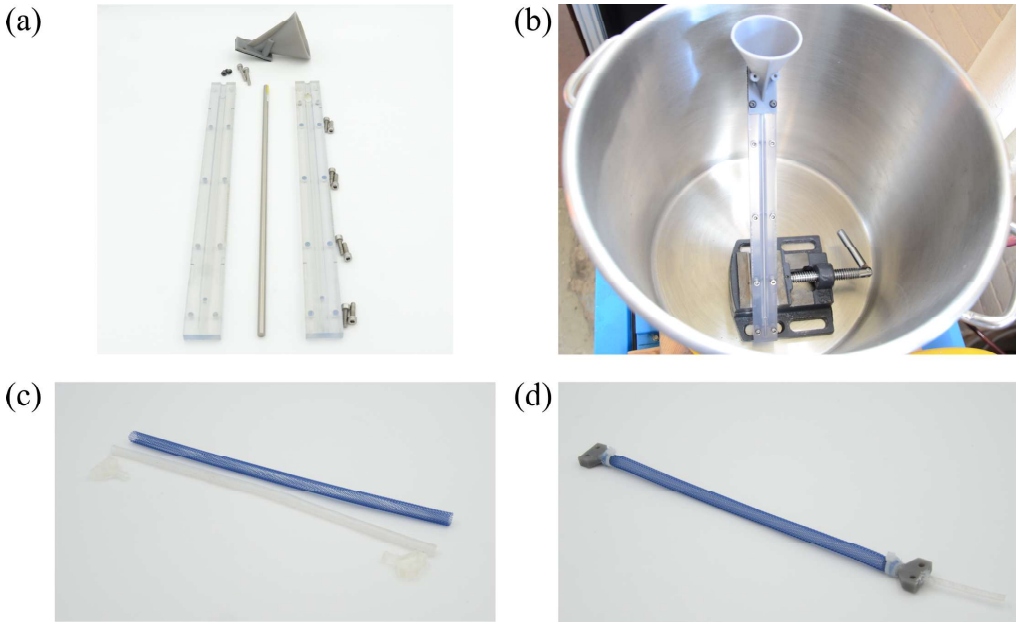

Fig. 10. Selected images from the manufacturing process. (a) Disassembled mold. (b) Assembled mold in place in the degassing chamber. (c) Actuator tube, sheath and caps prior to assembly. (d) Assembled actuator.